Phase diagram of the Hubbard model on a square lattice: A cluster slave-spin study

Ming-Huan Zeng, Tianxing Ma,* and Y.-J. Wang†
Department of Physics, Beijing Normal University, Beijing 100875, China

(Received 15 June 2021; revised 22 September 2021; accepted 22 September 2021; published 29 September 2021)

The cluster slave-spin method is employed to investigate systematically the ground state properties of the Hubbard model on a square lattice with doping δ and coupling strength U being its parameters. At half-filling, a relation between the staggered magnetization M and the antiferromagnetic (AFM) gap Δ_{AFM} is established in the small U limit to compare with that from the Hartree-Fock theory, and a first-order metal-insulator Mott transition in the paramagnetic state is substantiated, which is characterized by discontinuities and hystereses at $U_{\mathrm{Mott}} = 10t$. The interaction U_c for the crossover in the AFM state, separating the weak- and strong-coupling regimes, is found to remain almost unchanged with large dopings, and smaller than U_{Mott} at half-filling because of long range AFM correlations. Finally, an overall phase diagram in the U-δ plane is presented, which is composed of four regimes: the AFM insulator at half-filling, the AFM metal with the compressibility $\kappa > 0$ or $\kappa < 0$, and the paramagnetic metal, as well as three phase transitions: (i) From the AFM metal to the paramagnetic metal, (ii) between the AFM metal phases with positive and negative κ, and (iii) separating the AFM insulating phase at $\delta = 0$ from the AFM metal phase for $\delta > 0$.

DOI: 10.1103/PhysRevB.104.094524

I. INTRODUCTION

Because of its intimate relation to the high-T_c unconventional superconductivity based on cuprate oxides, the one-band Hubbard model [1] on a square lattice has been extensively studied through many theoretical approaches—Green's function methods [1–4], slave-variable representations [5–10], variational methods for the wave functions and spin configurations [11–15], renormalization-group methods [16–19], and numerical methods such as the quantum Monte Carlo (QMC) simulations [20–28], cluster dynamical mean-field theory (CDMFT) [29–31], density matrix embedding theory (DMET) [32,33], etc. Up till now, some consensuses about this model have been reached, e.g., the first-order metal-insulator Mott transition in the half-filled paramagnetic (PM) state [19,29,34–38] and an infinitesimal critical coupling strength for the antiferromagnetic (AFM) phase at half-filling because of the nested Fermi surface in the square lattice [2,3,5,20–23,32,39–44]. Even if the Mott transition in the half-filled PM system transforms into a crossover in the AFM state [21,22,26], the relationship between them has not yet been understood thoroughly. There are two types of phase separation: the one with hole-rich and hole-poor regions [21,27,28] and that with incommensurate AFM [45] at small and intermediate U. While the earlier works [46–48] present the phase separation as a mixture of AFM and FM states in the large U limit, we find that the phase separation happens easier when doping the AFM Slatter insulator. It is worthy of noticing that the theoretical and numerical results cannot be compared with experiments on the cuprate oxides directly because some crucial simplifications have been made in the Hubbard model by neglecting the long range Coulomb interaction, the hopping matrix elements further than the nearest neighbors, and the interlayer correlations, which have made the phase diagram of the two-dimensional (2D) Hubbard model [4,21] qualitatively different from that of high-T_c cuprate superconductors [49]. However, recent experimental improvement on the ultracold atoms to lower the local temperature of the optical lattice beyond the exchange energy J make it possible to observe the spatial charge and spin correlations even beyond the nearest neighbors [50–52]. Thus, the optical lattice platform could not only help us unveil the phase diagram in the intriguing regime where the kinetic energy and interaction potential become comparable, but also examine the validity of various theoretical methods based on different approximations. Meanwhile, more reliable results of the model ought to be needed to provide guidelines for experimental researches.

Although the QMC method have succeeded in coping with the half-filled bipartite lattice, the sign problem for the doped fermion systems and the finite size effect make its predictions for non-half-filled systems at least questionable. In these cases, some nonperturbative semianalytic methods based on slave-variable representations have been introduced to throw some light on the regime with modest coupling strengths, where the conventional perturbative techniques fail to give rise to correct solutions. Among all the slave-particle approaches, slave-boson method has been applied to the single band [5] and multiorbital systems successfully [6]. Earlier, Kotliar and Rukenstein have proven that [5] the saddle point approximation within the slave-boson approach could reproduce the Gutzwiller approximation's results of the half-filled PM state, and high-energy excitations can be taken into account by the fluctuations around the saddle point. Nevertheless, as the dimension of degrees of freedom increases, the exponentially growing number of bosonic slave variables makes the slave

*txma@bnu.edu.cn
†yjwang@bnu.edu.cn

boson approach particularly inapplicable to multiorbital systems and cluster mean-field theories. For the large U Hubbard model, a fermion-spin transformation [10] has been developed to implement the charge-spin separation in its equivalent t-J model, where the charge degree of freedom is represented by a spinless fermion while the spin degree of freedom by a hard-core boson. Within this scheme and its development, both the normal state properties and superconductivity mechanism of doped cuprates has been investigated extensively [53].

Recently, the slave-spin approach [54–57] has been devised to study the half-filled multiorbital Hubbard model, where the slave spin is introduced to represent the charge sector of an electron. The difficulty mentioned above has been overcome because only one slave variable is needed for each degree of freedom. After that, the slave-spin method was improved by Hassan and de' Medici [7] to deal with the non-half-filled systems, known as the Z_2 slave-spin theory. However, it has been proven that the Z_2 slave-spin theory fails to reproduce the noninteracting dispersion of the multiorbital Hamiltonian because of the nonzero orbit-dependent Lagrange multipliers. Not only can the $U(1)$ slave-spin theory produce the same results as the Z_2 theorys when the on-site interaction is on, but also capture the correct dispersion in the noninteracting limit by the extra orbit-dependent effective chemical potential, which is identical to the Lagrange multiplier at $U = 0$ (see Appendix C for details). A recently generalized cluster slave-spin method [9] has succeeded in describing the crossover of the AFM gap Δ_{AFM} and obtaining the correct quasiparticle residue that is consistent with the extended Gutzwiller factor [12]. However, there remain some insufficiencies: (i) The solutions at $U < 5t$ are absent. (ii) They have not discussed the relationship between the crossover of the AFM gap and the Mott transition in the half-filled PM state. (iii) The properties of the charge component represented by the slave-spin variables have not been studied on the same footing as the spin degree of freedom. (iv) The phase diagram in the U-δ plane has not been given, which can provide us a holistic understanding of the ground state properties. (v) No attention has been paid to the half-filled system. By completing the missing parts mentioned above, we offer an overall phase diagram in the U-δ plane that consists of four regimes: AFM insulator, AFM metallic phases with positive and negative compressibility, and the PM metal. The first-order Mott transition occurs in the half-filled PM state, characterized by discontinuities and hystereses at $U = 10t$, which transforms into an extended crossover in the AFM state because of nonlocal AFM correlations. Besides, the phase separation, manifested by the negative compressibility, has been observed in the regions with intermediate dopings, indicating that the uniform AFM state is not the true ground state of the model.

The rest of this paper is organized as follows. In Sec. II we outline the cluster slave-spin mean-field theory of Ref. [9]. In Sec. III A the results of hole-doped systems obtained by the two/four-site cluster approximations are discussed comprehensively. In Sec. III B, for the half-filled system, we establish an analytical relation between M and Δ_{AFM} in the small U limit, and observe the first-order Mott transition in the PM state. In Sec. III C M, Δ_{AFM}, and the compressibility κ as functions of U and δ are studied thoroughly, and an overall phase diagram in the U-δ plane is presented.

II. FORMALISM

We start from the standard single-band fermionic Hubbard model [1] defined by

$$H = -t\sum_{\langle i,j\rangle\sigma}(c^{\dagger}_{i\sigma}c_{j\sigma} + \mathrm{H.c.}) + U\sum_{i} n_{i\uparrow}n_{i\downarrow} - \mu\sum_{i\sigma} n_{i\sigma}, \tag{1}$$

where t, U, μ are the nearest hopping constant, the on-site Coulomb repulsion energy, and the chemical potential, respectively. $\langle i, j\rangle$ represents that the sum is over the nearest neighbors, and $c_{i\sigma}$ ($c^{\dagger}_{i\sigma}$) annihilates (creates) an electron at site i with spin $\sigma =\uparrow, \downarrow$, and the number operator $n_{i\sigma} = c^{\dagger}_{i\sigma}c_{i\sigma}$.

In the slave-spin method, the electron operator c_{α} is decomposed into the product of a fermionic spinon and a slave spin with $S = \frac{1}{2}$ which represents the physical spin and charge degrees of freedom, respectively,

$$c^{\dagger}_{\alpha} = S^{\dagger}_{\alpha}f^{\dagger}_{\alpha}. \tag{2}$$

With the constraint $a^{\dagger}_{\alpha}a_{\alpha} + b^{\dagger}_{\alpha}b_{\alpha} = 1$, the slave-spin operator is rewritten in the Schewinger boson representation

$$S^{\dagger}_{\alpha} = a^{\dagger}_{\alpha}b_{\alpha}, \quad S^{z}_{\alpha} = \tfrac{1}{2}(a^{\dagger}_{\alpha}a_{\alpha} - b^{\dagger}_{\alpha}b_{\alpha}), \tag{3}$$

which has been utilized to describe the metal-insulator Mott transition in the multiorbital Hubbard model [8]. In the slave-spin formalism, the original Hillbert space of a single degree of freedom with the basis $\{|n_{\alpha}\rangle\} = \{|0\rangle, |1\rangle\}$ is enlarged to $\{|n^{f}_{\alpha}, S^{z}_{\alpha}\rangle\} = \{|0, -\frac{1}{2}\rangle, |1, \frac{1}{2}\rangle, |0, \frac{1}{2}\rangle, |1, -\frac{1}{2}\rangle\}$. Thus, the following constraint is enforced to project out the unphysical states $|0, \frac{1}{2}\rangle, |1, -\frac{1}{2}\rangle$:

$$S^{z}_{\alpha} = f^{\dagger}_{\alpha}f_{\alpha} - \tfrac{1}{2}. \tag{4}$$

However, according to Kotliar and Ruckenstein [5], the slave-spin operators defined in Eq. (3) need to be dressed to ensure the correct behavior in the noninteracting limit

$$\tilde{S}^{\dagger}_{\alpha} = P^{\dagger}_{\alpha}a^{\dagger}_{\alpha}b_{\alpha}P_{\alpha},$$
$$P^{\pm}_{\alpha} = \frac{1}{\sqrt{1/2 \pm S^{z}_{\alpha}}}. \tag{5}$$

Then, in the slave-spin method, the Hamiltonian (1) can be rewritten as

$$\begin{aligned} H = &-t\sum_{\langle i,j\rangle\sigma}(\tilde{S}^{+}_{i\sigma}f^{\dagger}_{i\sigma}\tilde{S}^{-}_{j\sigma}f_{j\sigma} + \mathrm{H.c.}) - \mu\sum_{i\sigma} f^{\dagger}_{i\sigma}f_{i\sigma} \\ &- \sum_{i\sigma}\lambda_{i\sigma}\left(f^{\dagger}_{i\sigma}f_{i\sigma} - S^{z}_{i\sigma} - \frac{1}{2}\right) \\ &+ \frac{U}{2}\sum_{i\sigma}\left(S^{z}_{i\sigma} + \frac{1}{2}\right)\left(S^{z}_{i-\sigma} + \frac{1}{2}\right), \end{aligned} \tag{6}$$

where the constraint (4) is taken care of by introducing a Lagrange multiplier $\lambda_{i\sigma}$. Under the two-site cluster approximation sketched in Fig. 1(a), Eq. (6) can be decomposed into a fermionic spinon Hamiltonian and a cluster slave-spin Hamiltonian as

$$H^{f}_{\mathrm{MF}} = \sum_{\langle i,j\rangle\sigma}[-tZ - \delta_{ij}(\mu + \lambda_{I\sigma} - \tilde{\mu}_{I\sigma})]f^{\dagger}_{i\sigma}f_{j\sigma} + \mathrm{H.c.}, \tag{7}$$

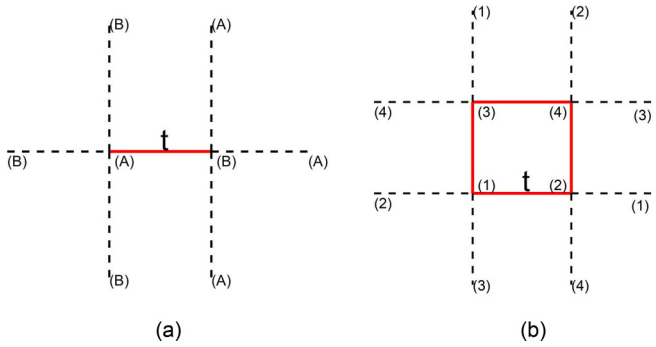

FIG. 1. Schematic illustration of the (a) two- and (b) four-site cluster.

$$
\begin{aligned}
H^S_{2\text{-site}} = & \sum_\sigma \left[\lambda^+_\sigma \left(S^z_{A\sigma} + S^z_{B\sigma}\right) + \lambda^-_\sigma \left(S^z_{A\sigma} - S^z_{B\sigma}\right)\right] \\
& + \sum_\sigma \left\{\epsilon^x_\sigma (\tilde{z}^\dagger_{A\sigma}\tilde{z}_{B\sigma} + \tilde{z}^\dagger_{B\sigma}\tilde{z}_{A\sigma}) \right. \\
& \left. + \left(\epsilon^x_\sigma + 2\epsilon^y_\sigma\right)[\tilde{z}^\dagger_{A\sigma}\langle\tilde{z}_{B\sigma}\rangle + \tilde{z}^\dagger_{B\sigma}\langle\tilde{z}_{A\sigma}\rangle + \text{H.c.}]\right\} \\
& + U\left(S^z_{A\uparrow} + \frac{1}{2}\right)\left(S^z_{A\downarrow} + \frac{1}{2}\right) \\
& + U\left(S^z_{B\uparrow} + \frac{1}{2}\right)\left(S^z_{B\downarrow} + \frac{1}{2}\right), \qquad (8)
\end{aligned}
$$

where $I = A/B$ and

$$
\begin{aligned}
& Z = \langle\tilde{z}^\dagger_{A\sigma}\rangle\langle\tilde{z}_{B\sigma}\rangle, \quad \lambda^\pm_\sigma = \frac{\lambda_{A\sigma} \pm \lambda_{B\sigma}}{2}, \\
& \tilde{\mu}_{I\sigma} = \frac{4Z\langle S^z_{I\sigma}\rangle\left(\epsilon^x_\sigma + \epsilon^y_\sigma\right)}{\left(\frac{1}{2}\right)^2 - \langle S^z_{I\sigma}\rangle^2}, \quad \epsilon^{x/y}_\sigma = -t\langle f^\dagger_{i\sigma} f_{i+\hat{x}/\hat{y}\sigma}\rangle. \qquad (9)
\end{aligned}
$$

The spinon part is readily Fourier transformed into $\boldsymbol{k}$ space:

$$
H^f_{\text{MF}} = \sum_{\boldsymbol{k},\sigma} (\xi_{\boldsymbol{k}\sigma} f^\dagger_{\boldsymbol{k}\sigma} f_{\boldsymbol{k}\sigma} + \Delta_\sigma f^\dagger_{\boldsymbol{k}\sigma} f_{\boldsymbol{k}+\boldsymbol{Q}\sigma}), \qquad (10)
$$

where

$$
\begin{aligned}
& \xi_{\boldsymbol{k}\sigma} = -4tZ\gamma_{\boldsymbol{k}} - \mu^{\text{eff}}, \quad \gamma_{\boldsymbol{k}} = \tfrac{1}{2}(\cos k_x + \cos k_y), \\
& \mu^{\text{eff}} = \mu - \tfrac{1}{2}(\tilde{\mu}_{A\sigma} - \lambda_{A\sigma} + \tilde{\mu}_{B\sigma} - \lambda_{B\sigma}), \qquad (11) \\
& \Delta_\sigma = \tfrac{1}{2}(\tilde{\mu}_{A\sigma} - \lambda_{A\sigma} - \tilde{\mu}_{B\sigma} + \lambda_{B\sigma}).
\end{aligned}
$$

Noticing that $\Delta_\sigma = -\Delta_{-\sigma}$ in the AFM state, the PM state can be reached by simply forcing the AFM gap $\Delta_{\text{AFM}} = |\Delta_\sigma| = 0$.

Still, there are two key points needed to be cleared. First, the fermionic spinon Hamiltonian (7) is very similar to that in the Hartree-Fock (HF) approximation except the hopping constant t is renormalized by the quasiparticle residue Z as tZ. Second, the Hamiltonian (8) in the slave-spin sector is a repulsively interacting Bose-Hubbard model for bosons $a_{i\sigma}$ and $b_{i\sigma}$ in the staggered external field $\lambda_{A\sigma}$ and $\lambda_{B\sigma}$. When the composite boson fields $\tilde{z}_{i\sigma}$ condensate, i.e., $\langle\tilde{z}_{i\sigma}\rangle \neq 0$ below the critical coupling strength U_{Mott} for the metal-insulator transition in the PM state, the system changes from the insulating phase to a metallic one [8]. Moreover, when U is strong enough to make $\lambda_{A\sigma} \neq \lambda_{B\sigma}$, i.e., $\lambda^-_\sigma \neq 0$, the system will transit into the AFM state from the PM state. Thus, the Hamiltonians (7) and (8) can describe both the Mott transition at $U = U_{\text{Mott}}$ in the PM phase and the PM-to-AFM transition at U_M.

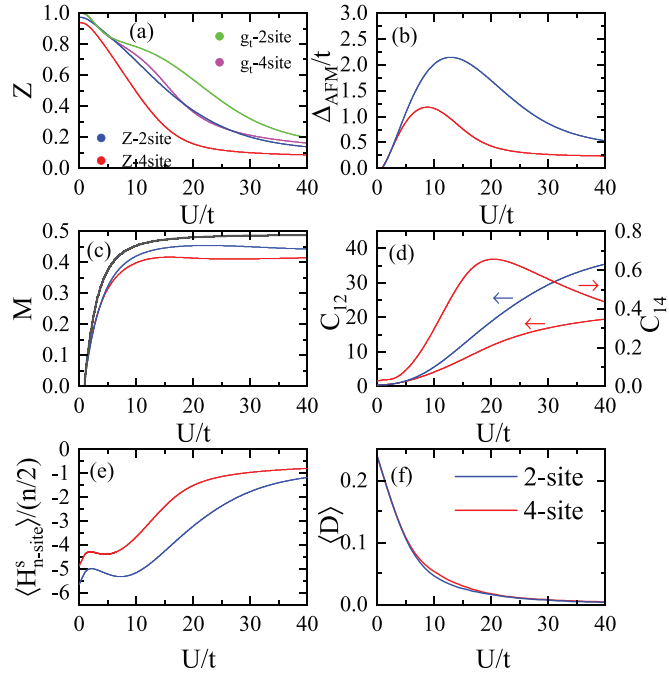

FIG. 2. (a) The quasiparticle weight Z and the generalized Gutzwiller factor g_t, (b) the AFM energy gap Δ_{AFM}/t, (c) the staggered magnetization M, (d) the holon-doublon correlator between the nearest neighbors C_{12} and the next nearest neighbors C_{14}, (e) the expectation value of the cluster slave-spin Hamiltonian $\langle H^S_{2\text{-site}}\rangle$ and $\langle H^S_{4\text{-site}}\rangle/2$, and (f) the double occupancy $\langle D\rangle$ as functions of U at $\delta = 0.02$ in the AFM state obtained by the two-site (blue) and the four-site (red) cluster. For comparison, the staggered magnetization within the HF theory at $\delta = 0.02$ is plotted in (c) as a black line.

It has been proven that the four-site cluster approximation makes a great improvement compared to the two-site one by including more intersite fluctuations [9]. Thus, except Figs. 2 and 9, all our results are obtained in the four-site cluster approximation as illustrated in Fig. 1(b), whose mean-field fermionic spinon Hamiltonian remains the same as Eq. (7), and the cluster slave-spin Hamiltonian reads

$$
H^S_{4\text{-site}} = H^S_\lambda + H^S_U + H^S_K, \qquad (12)
$$

where

$$
H^S_\lambda = \sum_{I=1\sigma}^{4} \lambda_{I\sigma} S^z_{I\sigma}, \qquad (13)
$$

$$
H^S_U = \sum_I U\left(S^z_{I\sigma} + \frac{1}{2}\right)\left(S^z_{I\bar{\sigma}} + \frac{1}{2}\right), \qquad (14)
$$

$$
\begin{aligned}
H^S_K = & \sum_\sigma \left\{\epsilon^x_\sigma (\tilde{z}^\dagger_{1\sigma}\tilde{z}_{2\sigma} + \tilde{z}^\dagger_{3\sigma}\tilde{z}_{4\sigma}) + \epsilon^y_\sigma (\tilde{z}^\dagger_{1\sigma}\tilde{z}_{3\sigma} + \tilde{z}^\dagger_{2\sigma}\tilde{z}_{4\sigma}) \right. \\
& + \epsilon^x_\sigma [\tilde{z}^\dagger_{1\sigma}\langle\tilde{z}_{2\sigma}\rangle + \tilde{z}^\dagger_{2\sigma}\langle\tilde{z}_{1\sigma}\rangle + \tilde{z}^\dagger_{3\sigma}\langle\tilde{z}_{4\sigma}\rangle + \tilde{z}^\dagger_{4\sigma}\langle\tilde{z}_{3\sigma}\rangle] \\
& + \epsilon^y_\sigma [\tilde{z}^\dagger_{1\sigma}\langle\tilde{z}_{3\sigma}\rangle + \tilde{z}^\dagger_{3\sigma}\langle\tilde{z}_{1\sigma}\rangle + \tilde{z}^\dagger_{2\sigma}\langle\tilde{z}_{4\sigma}\rangle + \tilde{z}^\dagger_{4\sigma}\langle\tilde{z}_{2\sigma}\rangle] \\
& \left. + \text{H.c.}\right\}. \qquad (15)
\end{aligned}
$$

In this work, we only investigate the ground state properties of the system and will adopt the following density of states in

all computations to avoid the finite size effect,

$$D(\gamma) = \frac{1}{N}\sum_{k}\delta(\gamma - \gamma_k) = \frac{2}{\pi^2}K(\sqrt{1-\gamma^2}), \qquad (16)$$

where $K(x)$ is the complete elliptical function of the first kind.

III. RESULTS AND DISCUSSIONS

A. Systems with finite doping

We analyze the quasiparticle residue Z, the generalized Gutzwiller factor g_t [9,12,58], the AFM gap $\Delta_{\rm AFM}$, the staggered magnetization M, the holon-doublon correlators between the nearest neighbors C_{12} and the next nearest neighbors C_{14} [cf. (A1) for definition], the ground state energy of the slave-spin Hamiltonian $\langle H^S_{\text{2-site}}\rangle$, $\langle H^S_{\text{4-site}}\rangle/2$, and the double occupancy $\langle D\rangle$ as functions of U at $\delta = 0.02$ obtained from the two- and four-site cluster approximations in Fig. 2.

The results are as follows: (i) In Fig. 2(a) we find that Z's behave similarly with g_t in both the two- and four-site cluster approximations, and it is suppressed drastically when extra intersite fluctuations are taken into account as the cluster size is enlarged from two to four. (ii) In Fig. 2(b) the crossover U_c separating the weak- and strong-coupling regime in the AFM state is defined by the peak position of $\Delta_{\rm AFM}$, which decreases from $12.9t$ (two site) to $8.9t$ (four site). Both $\Delta_{\rm AFM}$ and M [Fig. 2(c)] are restrained appreciably by the intersite fluctuations. One observes that M from the cluster slave-spin approximation and the HF theory are consistent when U is small. (iii) In Fig. 2(d) a maximum of C_{14} around $U \sim 20t$ can be identified as one of the features of the strong correlation, the reason for which has been analyzed in Appendix A. (iv) In Fig. 2(e) $\langle H^S_{n\text{-site}}\rangle/(n/2)$ in the AFM states declines suddenly at $U \sim U_M \sim t$, which is caused by the decrease of the interaction potential compared to the PM state in this region [cf. Fig. 3(f)], and behaves as $-1/U$ at large U, which is similar to $\Delta_{\rm AFM}/t$. (v) In Fig. 2(f), as U goes up, the double occupancy decreases monotonically, which probably tends to zero as U goes to infinity. Finally, we find that the difference between the results from two approximations is much smaller in the small and large U limit than those at intermediate U's, which necessitates enlarging the cluster size to study the properties of Hubbard model with moderate coupling strengths.

To understand how the quantities discussed in Fig. 2 evolve with the increase of U at different doping levels, their dependence on U at a set of dopings $\delta^P = 0.02$, $\delta^A = 0.02, 0.05, 0.1, 0.2$ are plotted in Fig. 3, where A and P denote the AFM or PM state, respectively. First, in Fig. 3(a), we find that Z in the PM state is larger than its counterpart in the AFM state when $U < 6t$, or otherwise when $U > 6t$, and the quasiparticle weight in the PM state decreases more dramatically than that in the AFM state around $U \sim U_{\rm Mott} = 10t$ at $\delta = 0.02$. Moreover, the increase of Z with doping in the AFM state is observed at all U's, signifying the system's tendency towards a correlated metal. Second, the $\Delta_{\rm AFM}$ at all dopings present a crossover behavior at U_c and then reaches a finite value except for $\delta = 0.2$ whose $\Delta_{\rm AFM}$ vanishes at $U = 26t$ in Fig. 3(b). The reason for this unusual behavior may be that at $\delta = 0.2$, the system is an AFM metal, whereas the increased U makes the system more localized which is unfavorable to

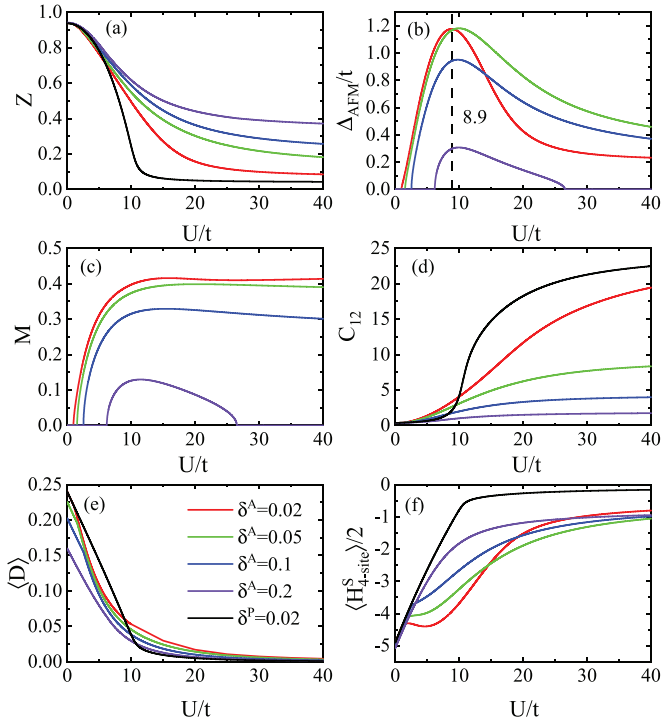

FIG. 3. (a) The quasiparticle weight Z, (b) the AFM energy gap $\Delta_{\rm AFM}/t$, (c) the staggered magnetization M, (d) the holon-doublon correlator between the nearest neighbors C_{12}, (e) the double occupancy per site, and (f) the expectation value of the cluster slave-spin Hamiltonian as functions of U at a set of doping concentrations $\delta = 0.02$ (red), 0.05 (green), 0.1 (blue), 0.2 (violet) in the AFM state and $\delta = 0.02$ (black) in the PM state obtained by the four-site cluster.

the itinerant AFM. It is worth mentioning that $\Delta_{\rm AFM}$ shows a nonmonotonic behavior with the increase of doping when $U > U_{\rm Mott}$. Third, as shown in Fig. 3(c), M decreases monotonically with doping and like $\Delta_{\rm AFM}$ at $\delta = 0.2$, the staggered magnetization also vanishes after reaching its maximum at U_c. The same picture has been observed in the recent DMET calculation [32] and some earlier work by Kotliar and Ruckenstein [5]. The holon-doublon correlator C_{12} and double occupancy $\langle D\rangle$ as functions of U are depicted in Figs. 3(d) and 3(e), respectively, both of which decrease monotonically with δ. C_{12} in the PM state is smaller than that in the AFM state when $U < U_c$ ($8.9t$ for $\delta = 0.02$), or otherwise in the case of $U > U_c$, while the opposite is true for $\langle D\rangle$. Furthermore, the ground state energy of the cluster slave-spin Hamiltonian (12) $\langle H^S_{\text{4-site}}\rangle/2$ is plotted in Fig. 3(f). There are three key points needed to be addressed: (i) According to Fig. 3(e), compared to the PM state, it is the decrease of the interaction potential that makes $\langle H^S_{\text{4-site}}\rangle/2$ decline rapidly upon entering the AFM state. (ii) For $U \lesssim U_{\rm Mott} = 10t$, $\langle H^S_{\text{4-site}}\rangle/2$ increases monotonically with doping, while it presents a nonmonotonic behavior when $U \gtrsim U_{\rm Mott}$. (iii) In contrast to the PM state, $\langle D\rangle$ and $\langle H^S_{\text{4-site}}\rangle/2$ diminish drastically as the AFM emerges, which can be understood through $\langle D_i\rangle = (1-\delta)/2 - 2\langle M_i^2\rangle$ with $M_i = (n_{i\uparrow} - n_{i\downarrow})/2$.

We now discuss the difference of the energetics of the slave-spin Hamiltonian (12) between the AFM and PM states, as well as the electron momentum distribution and

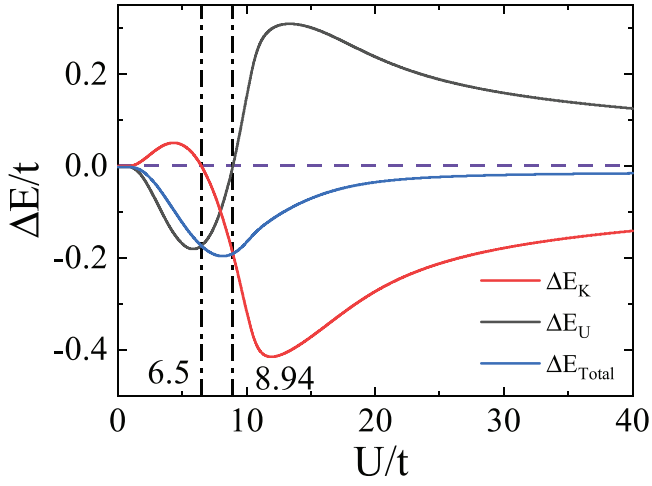

FIG. 4. The difference of the kinetic energy, interaction potential, and the total energy of the cluster slave-spin Hamiltonian between the AFM and PM state as functions of U at $\delta = 0.02$ obtained by the four-site cluster.

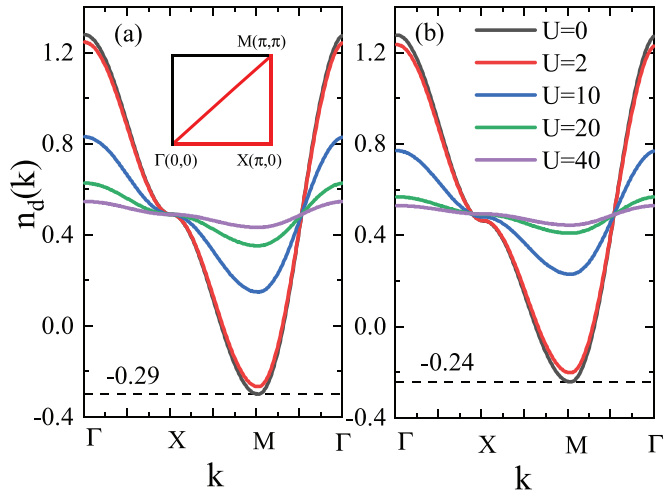

FIG. 5. (a) and (b) The electron momentum distribution $n_d(\boldsymbol{k})$ versus U at $\delta = 0.02$ obtained by the two- and four-site cluster, respectively.

the hopping probability between the nearest and next nearest neighbors.

The differences of the kinetic energy E_K, interaction potential E_U, and their summation E_{Total} of the approximate Hamiltonian (12) between the AFM and PM states ($\Delta E = E^{(A)} - E^{(P)}$) as functions of U are plotted in Fig. 4. We observe a region around $6.5t < U < 8.94t$ separating the weak- and strong-coupling regimes in the AFM state [21,22,26,29,59]. When $U < 6.5t$ or $U > 8.94t$, the AFM state in the system is governed by the interaction potential gain supporting the Slater mechanism or the kinetic energy gain that favors the superexchange mechanism, respectively [21,30,59]. However, a sharp crossover is observed at U_{Mott} in the recent CDMFT calculation of the half-filed Hubbard model [30].

The electron momentum distribution $n_d(\boldsymbol{k})$ calculated in Appendix B are plotted in Figs. 5(a) and 5(b). The overall feature is that the on-site interaction transfers the electrons within the Fermi surface outside and the tendency is strengthened by the stronger interaction, which is consistent with the result of QMC simulation [23]. However, we fail to reproduce the standard Fermi surface even in the noninteracting limit, and $n_d(\boldsymbol{k})$ is larger than unity at $\boldsymbol{k} = (0, 0)$ and negative at $\boldsymbol{k} = (\pi, \pi)$ in both two- and four-site cluster approximations, whereas an improvement can be seen when the cluster size is enlarged. This kind of failure reflects an intrinsic flaw in all slave-variables approaches [60].

The hopping probability between the nearest neighbor $|\langle c^{\dagger}_{i\sigma} c_{i+\delta\sigma}\rangle|^2 \approx Z^2 |\langle f_{i\sigma} f_{i+\delta\sigma}\rangle|^2$ and its derivative are plotted in Figs. 6(a) and 6(b).$|\langle c^{\dagger}_{i\sigma} c_{i+\delta\sigma}\rangle|^2$ is smaller in the AFM state than in the PM state when $U_M < U < U_c$, because the AFM state is driven by the interaction potential gain at small U (see Fig. 4) that suppresses the double occupancy, leading to the same effect on $|\langle c^{\dagger}_{i\sigma} c_{i+\delta\sigma}\rangle|^2$ [compare Figs. 3(e) and 6(a)]. However, the opposite is true when $U > U_c$ because the AFM state is stabilized by the superexchange mechanism at large U. Accordingly, the gradient of $|\langle c^{\dagger}_{i\sigma} c_{i+\delta\sigma}\rangle|^2$ with respect to U has a minimum at $U = 3.0t$, $7.4t$ in the AFM and PM states, respectively, signifying that the long range AFM order suppresses the hopping probability between the nearest neighbors noticeably for small U.

The hopping probability between the next nearest neighbors $|\langle c^{\dagger}_{i\sigma} c_{i+\delta'\sigma}\rangle|^2$ $(i \in A) \approx |\langle \tilde{z}_{A\sigma}\rangle|^4 \langle f_{i\sigma} f_{i+\delta'\sigma}\rangle|^2$ and its derivative are shown in Figs. 7(a) and 7(b). In the AFM state, $|\langle c^{\dagger}_{i\sigma} c_{i+\delta'\sigma}\rangle|^2$ depends either on site i or on spin σ, and varies nonmonotonically—remaining small when $U < U_M$, then zooming up at $U = U_M$, and vanishing when $U > U_{\text{Mott}}$

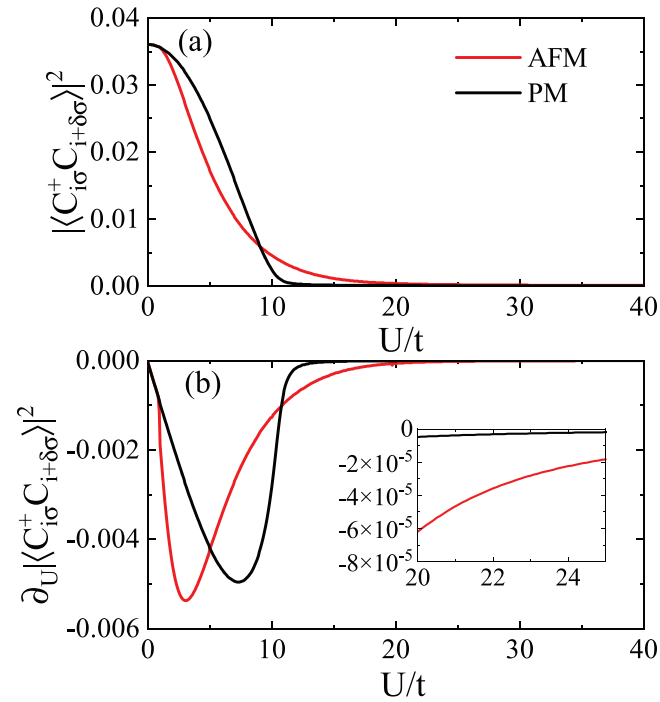

FIG. 6. (a) The hopping probability between the nearest neighbors $|\langle c^{\dagger}_{i\sigma} c_{i+\delta\sigma}\rangle|^2$ and (b) its derivative as functions of U at $\delta = 0.02$ in the AFM (red) and PM (black) states obtained by four-site cluster.

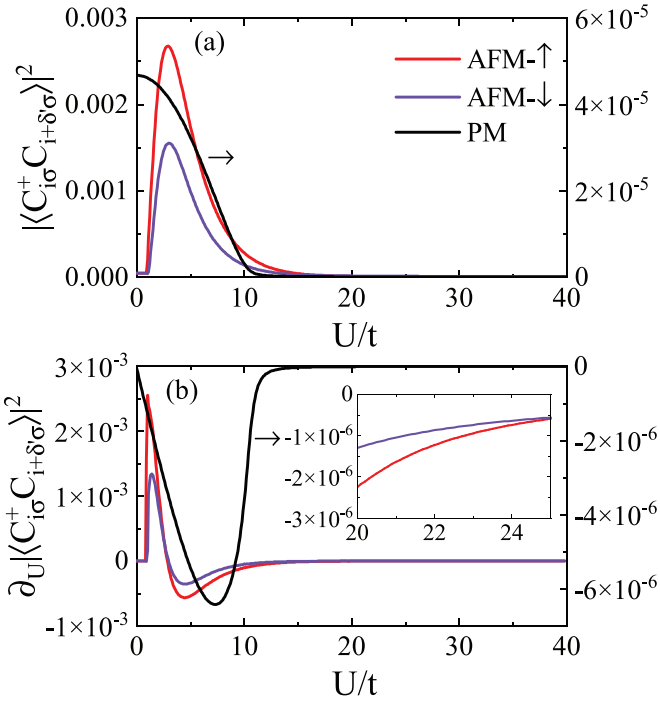

FIG. 7. (a) The hopping probability between the next nearest neighbors $|\langle c^\dagger_{i\sigma}c_{i+\delta'\sigma}\rangle|^2$ and (b) its derivative as functions of U at $\delta = 0.02$ in the AFM (red and violet) and PM (black) states obtained by four-site cluster.

after reaching its maximum at $U \sim 3t$. However, in the PM state, it decreases to zero monotonically as U increases.

B. Half-filled system

By diagonalizing the spinon Hamitonian (10), the self-consistent parameters $n^f_{A/B\sigma} \equiv \langle f^\dagger_{A/B\sigma} f_{A/B\sigma}\rangle$ and ϵ^δ_σ can be obtained:

$$\epsilon^\delta_\sigma = \epsilon = \frac{1}{2N}\sum_{\boldsymbol{k}} \frac{4t^2 Z\gamma_{\boldsymbol{k}}^2}{\sqrt{(4tZ\gamma_{\boldsymbol{k}})^2+\Delta_\sigma^2}}[\theta(-E^+_{\boldsymbol{k}}) - \theta(-E^-_{\boldsymbol{k}})], \tag{17}$$

$$n^f_{A/B\sigma} = \frac{1}{2N}\sum_{\boldsymbol{k}}\Bigg[\theta(-E^+_{\boldsymbol{k}}) + \theta(-E^-_{\boldsymbol{k}}) \mp \frac{\Delta_\sigma}{\sqrt{(4tZ\gamma_{\boldsymbol{k}})^2+\Delta_\sigma^2}}[\theta(-E^+_{\boldsymbol{k}}) - \theta(-E^-_{\boldsymbol{k}})]\Bigg], \tag{18}$$

where

$$E^\pm_{\boldsymbol{k}} = -\mu^{\text{eff}} \pm \sqrt{(4tZ\gamma_{\boldsymbol{k}})^2+\Delta_\sigma^2}. \tag{19}$$

At half-filling, the particle-hole symmetry ensures that $\mu^{\text{eff}} = 0$ and $E^+_{\boldsymbol{k}} > 0$. With the density of state (16), Eqs. (17) and (18) can be rewritten as

$$\begin{aligned}\epsilon &= -t\lambda\int_0^1 d\gamma D(\gamma)\gamma^2\frac{1}{\sqrt{(\lambda\gamma)^2+1}}\\ &= -t\lambda I_\epsilon(\lambda),\end{aligned} \tag{20}$$

$$\begin{aligned}n^f_{A/B\sigma} &= \frac{1}{2} \mp \text{sgn}(\Delta_\sigma)\int_0^1 d\gamma D(\gamma)\frac{1}{\sqrt{(\lambda\gamma)^2+1}}\\ &= \frac{1}{2} \mp \text{sgn}(\Delta_\sigma) I_f(\lambda) = \frac{1}{2} + \langle S^z_{A/B\sigma}\rangle,\end{aligned} \tag{21}$$

with $\lambda = 4tZ/\Delta_{\text{AFM}}$.

To establish the relation between M and Δ_{AFM} in the small U limit, we expand asymptotically the integrals $I_\epsilon(\lambda)$ and $I_f(\lambda)$ as $\lambda \to \infty$ [61]:

$$\epsilon \sim -t\left[\frac{2}{\pi^2} - \frac{\tilde\Delta^3(\ln\tilde\Delta)^2}{2\pi^2} - \left(\frac{1}{2\pi^2} - \frac{3\ln 2}{\pi^2}\right)\tilde\Delta^2\ln\tilde\Delta + \left(\frac{1}{4\pi^2} + \frac{3\ln 2}{2\pi^2} - \frac{9(\ln 2)^2}{2\pi^2}\right)\tilde\Delta^2\right], \tag{22}$$

$$\langle S^z_{A/B\sigma}\rangle \sim (-/+)\,\text{sgn}(\Delta_\sigma)\left[\frac{1}{\pi^2}\tilde\Delta(\ln\tilde\Delta)^2 - \frac{6\ln 2}{\pi^2}\tilde\Delta\ln\tilde\Delta + \frac{9(\ln 2)^2}{\pi^2}\tilde\Delta\right], \tag{23}$$

with $\tilde\Delta = \lambda^{-1} = \Delta_{\text{AFM}}/(4tZ)$, resulting in

$$M = \frac{1}{2}\left|\langle S^z_{A\sigma}\rangle - \langle S^z_{B\sigma}\rangle\right| \sim \frac{1}{\pi^2}\tilde\Delta(\ln\tilde\Delta)^2 - \frac{6\ln 2}{\pi^2}\tilde\Delta\ln\tilde\Delta + \frac{9(\ln 2)^2}{\pi^2}\tilde\Delta. \tag{24}$$

Therefore, the simple HF relation of $\Delta_{\text{AFM}} = UM$ [20] needs to be corrected. By adopting the U dependent form of the AFM gap

$$\Delta_{\text{AFM}} = A\sqrt{U}e^{-B\sqrt{\frac{1}{U}}}, \tag{25}$$

which has been verified by the QMC method [20], we fit our self-consistent data to obtain

$$\begin{aligned}A &= 0.02086 \pm 0.00418,\\ B &= 1.90604 \pm 0.06189,\end{aligned} \tag{26}$$

as shown in Fig. 8(a). Then, the result is substituted into Eq. (24) to recover perfectly the data of M shown Fig. 8(b).

Moreover, the AFM gap Δ_{AFM}, starting from an infinitesimal U, should also present in the spectrum function of the electron [22]. In the slave-spin method, the spectrum function of the electron Green's function can be expressed as [62]

$$A(\boldsymbol{q},\omega) = \int_{\boldsymbol{k}}\int_0^\omega d\Omega A_{\text{s-spin}}(\boldsymbol{q}-\boldsymbol{k},\omega-\Omega)A_{\text{fermion}}(\boldsymbol{k},\Omega). \tag{27}$$

Assuming a gap Δ_{AFM} in the fermionic spinon sector of Hamiltonian (1), $A_{\text{fermion}}(\boldsymbol{k},\Omega<\Delta_{\text{AFM}}) = 0$, it is easy to understand that the electron spectrum function $A(\boldsymbol{q},\omega)$ will vanish when ω is smaller than Δ_{AFM}.

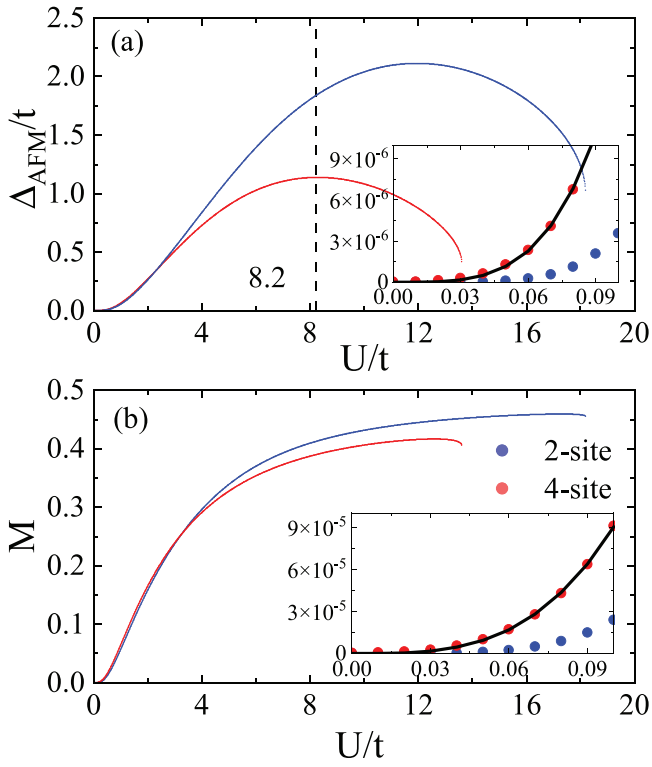

FIG. 8. (a) The AFM energy gap Δ_{AFM}/t where the inset shows the same data at small U together with the fitting data (black line) and (b) the staggered magnetization M where the inset shows the same data at small U together with that calculated by Eq. (24) (black line).

Additionally, Z, $C_{12/14}$, $\langle H^S_{4\text{-site}}\rangle/2$, and $\langle D\rangle$ as functions of U are plotted in Fig. 9. The overall features are similar to those with $\delta = 0.02$ (cf. Fig. 2 for comparison) except for two critical distinctions. First, in the PM state, the first-order Mott transition occurs at $U_{\mathrm{Mott}} = 10t$, characterized by the discontinuity and hysteresis behavior of these quantities [29,34,38,63]. Compared to the AFM's $U_c = 8.2t$ shown in Fig. 8(a), we find that the AFM correlations significantly reduce the coupling strength which separates the weak- and strong-coupling regimes. This is consistent with the CDMFT calculation [29]. Second, both the AFM solutions at large U obtained from the two/four-site cluster approximations are absent, and the quasiparticle residue drops abruptly when U approaches the critical coupling strength where the AFM solution happens to disappear, which may imply a transition between the Hubbard model with $Z \neq 0$ and Heisenberg model with $\Delta_{\mathrm{AFM}} = 0$, i.e., $Z = 0$. To justify this argument, notice the contribution to Δ_{AFM} comes from two parts [see Eq. (11)]: the differences of the effective chemical potentials $[\Delta^{\mu}_{\mathrm{AFM}} = \frac{1}{2}(\tilde{\mu}_{A\sigma} - \tilde{\mu}_{B\sigma})]$ and the lagrange multipliers $[\Delta^{\lambda}_{\mathrm{AFM}} = \frac{1}{2}(\lambda_{A\sigma} - \lambda_{B\sigma})]$ between sublattice A and B, i.e., $\Delta_{\mathrm{AFM}} = \Delta^{\mu-\lambda}_{\mathrm{AFM}} = \Delta^{\mu}_{\mathrm{AFM}} - \Delta^{\lambda}_{\mathrm{AFM}}$, all of which as functions of U are plotted in Fig. 10. For comparison, those at $\delta = 0.02$ are presented too. One finds the main contribution to Δ_{AFM} is from $\Delta^{\mu}_{\mathrm{AFM}}$ [9], which is proportional to Z. From Fig. 10(a), both $\Delta^{\mu}_{\mathrm{AFM}}$ and $\Delta^{\lambda}_{\mathrm{AFM}}$ approach zero as Z vanishes, resulting in the disappearance of Δ_{AFM} at $U \sim 13.6t$, which may be connected to the gapless magnetic excitation of the Heisenberg model.

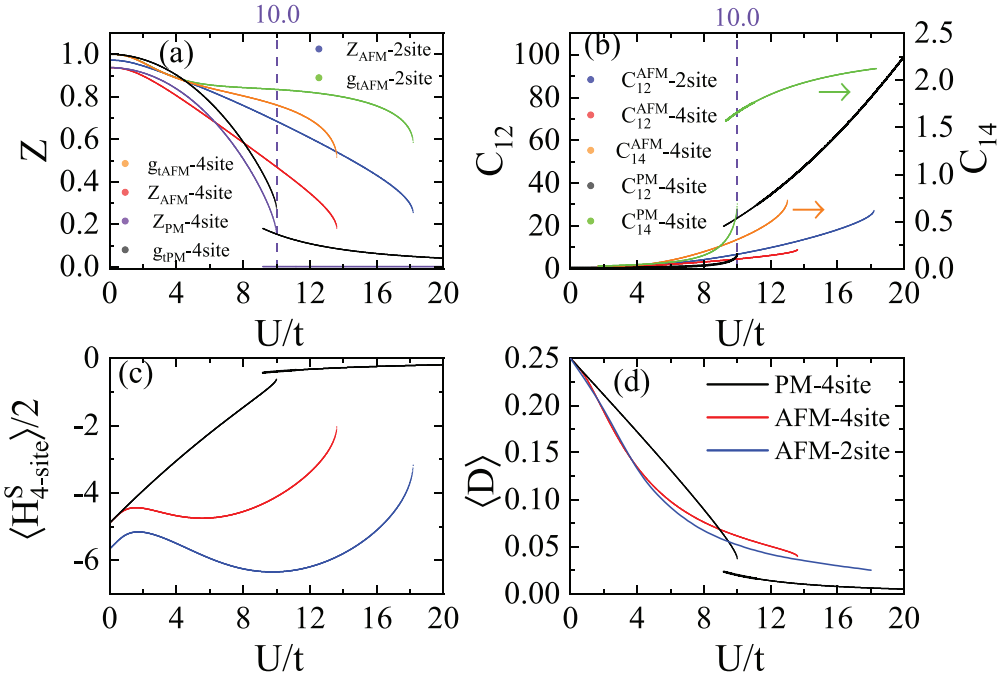

FIG. 9. (a) The quasiparticle weight Z and the generalized Gutzwiller factor g_t, (b) the holon-doublon correlators between the nearest neighbors C_{12} and the next nearest neighbors C_{14}, (c) the expectation value of the cluster slave-spin Hamiltonian, and (d) the double occupancy $\langle D\rangle$ in the AFM state as functions of U obtained by the two/four-site clusters (blue, red), respectively, and those in the PM state obtained by the four-site cluster (black).

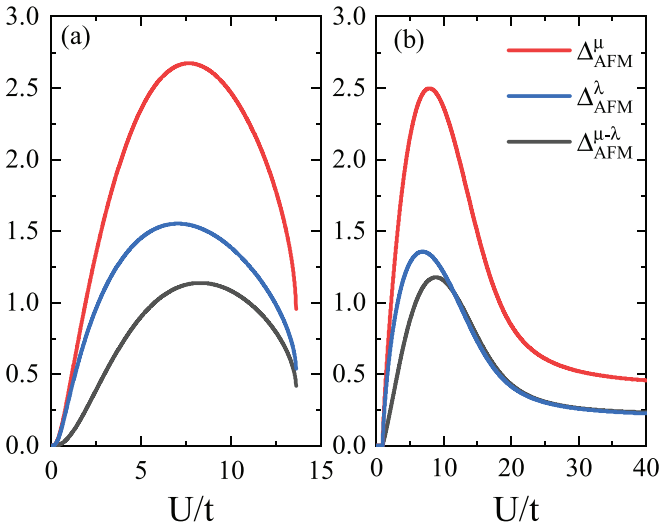

FIG. 10. The AFM gap Δ_{AFM}/t (black), $\Delta^{\mu}_{\mathrm{AFM}}/t$ (red), $\Delta^{\lambda}_{\mathrm{AFM}}/t$ (blue) as functions of U obtained from the four-site cluster at (a) $\delta = 0.0$ and (b) $\delta = 0.02$.

C. Phase diagram

In the following we combine the results of the staggered magnetization M (Fig. 11), the AFM gap Δ_{AFM} (Fig. 12), and the compressibility κ (Fig. 13) to present an overall phase diagram for the Hubbard model (Fig. 15).

The staggered magnetization M with δ and U being its parameters is plotted in Fig. 11, where the phase boundary between the AFM and PM states is denoted by $\delta_M(U)$. First, the staggered magnetization always saturates at a certain value when $U > U_{\mathrm{Mott}}$, while decreases monotonically with δ. Second, marked by the dense contours around $\delta_M(U)$, the staggered magnetization decreases continuously to zero as δ approaches $\delta_M(U)$, signifying the second-order transition between the AFM and the PM phases. Third, $\delta_M(U)$ shows a nonmonotonic behavior with U [31], which is consistent with the reentrance of M with U at $\delta = 0.2$, as shown in Fig. 3(c).

The AFM gap Δ_{AFM} in the same parameter space is plotted in Fig. 12, where the previous boundary $\delta_M(U)$ still holds for

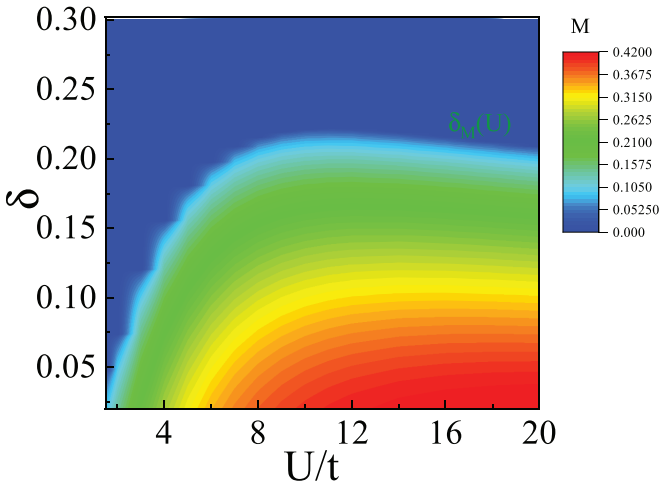

FIG. 11. The staggered magnetization M as functions of U and δ in the AFM states obtained by the four-site cluster.

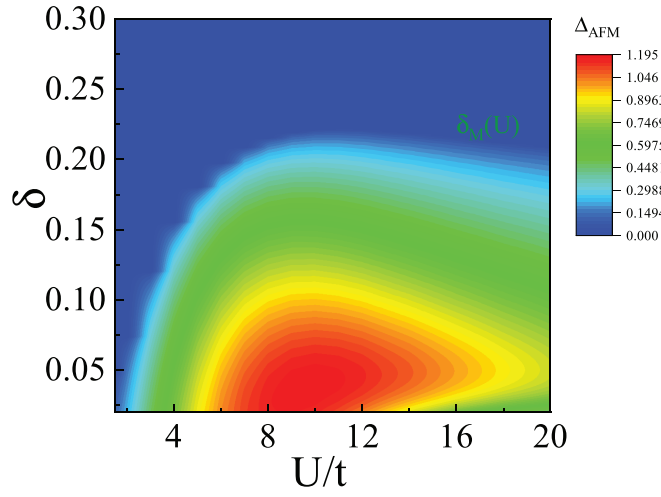

FIG. 12. The AFM gap Δ_{AFM} as functions of U and δ in the AFM states obtained by the four-site cluster.

Δ_{AFM}. When $U > U_{\mathrm{Mott}}$, the maximum of Δ_{AFM} occurs at $\delta \approx 0.05$, leading to the interesting vertical reentrance behavior as δ increases, which reflects that the AFM gap at half-filling vanishes in the large U limit.

Figure 13 shows the results for the compressibility $\kappa = n^{-2}\partial n/\partial\mu$. The staircase in this figure obviously is an artifact because of discrete U's adopted to calculate κ, i.e., $\Delta U = t$ when $U \leqslant 12t$ and $\Delta U = 2t$ when $12t < U \leqslant 20t$, which can only be eliminated in the $\Delta U \to 0$ limit. As shown in Fig. 13, there exist two phase boundaries delineated by the midpoints of these steps: (i) $\delta^1_\kappa(U)$, between the regions with positive (red) and negative (blue) compressibility. (ii) $\delta^2_\kappa(U)$, from the region with $\kappa < -0.5$ (blue) to $0.2 < \kappa < 0.5$ (yellow). As shown in Fig. 14, $\kappa = 0$ at half-filling is disconnected from that at an infinitesimal doping [31], signifying that the half-filled system in the AFM state is an insulator while the doped one a metal. By Figs. 11 and 13, the systems with $\delta^1_\kappa(U) < \delta < \delta^2_\kappa(U)$ are AFM metals with negative compressibility, meaning the uniform AFM configuration is not the

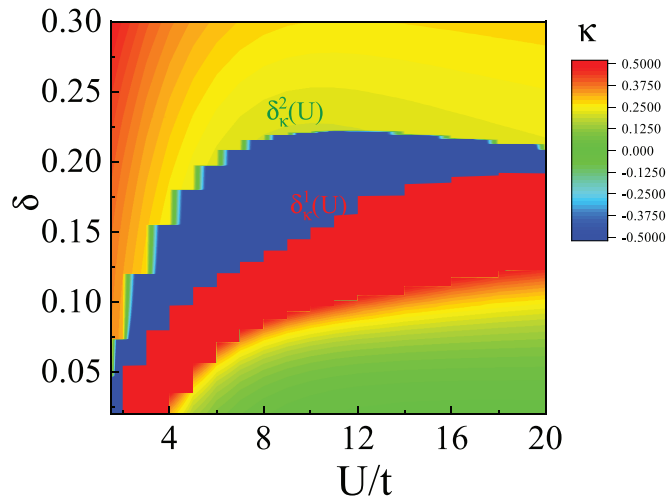

FIG. 13. The compressibility κ as functions of U and δ in the AFM states obtained by the four-site cluster. κ in the red and blue region are greater than 0.5 and less than -0.5, respectively.

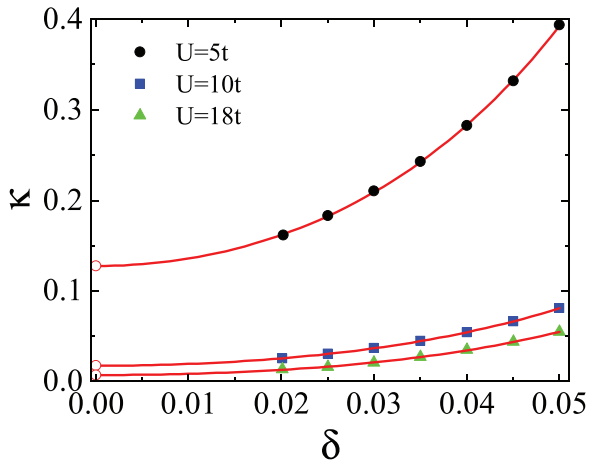

FIG. 14. The compressibility κ as functions of δ in the AFM state at $U = 5t$, $10t$, and $18t$ obtained by four-site cluster. Red lines are the extrapolated curves from the corresponding self-consistent data using $\kappa_0 + \alpha\delta^2 + \beta\delta^4$. The red circles at $\delta = 0$ denotes the discontinuity of $\kappa = 0$ at $\delta = 0$.

actual ground state, whereas an inhomogeneous phase with $M \neq 0$ could be the alternative [4,21,27,28,32]. In addition, the space between $\delta_\kappa^1(U)$ and $\delta_\kappa^2(U)$ shows a broadening-narrowing feature as U increases, and they may merge into one as $U \gg 20t$, implying that this kind of phase separation cannot be observed in the large U limit [21,27,28]. Moreover, $\delta_\kappa^2(U)$ is identical to $\delta_M(U)$, thus, $\delta_M(U)$ is the boundary separating the AFM metal phase with $\kappa < 0$ and the PM metal phase.

By aggregating Figs. 11, 12, and 13, we acquire an overall phase diagram, Fig. 15, of the Hubbard model in the U-δ plane. The boundary $\delta_{\rm HF}(U)$ between the AFM and PM phases within the HF theory is plotted as the dashed line. As expected, the consistency between $\delta_{\rm HF}(U)$ and $\delta_M(U)$ only lies in the small U region, which is also the case of M in Fig. 2(c). There exists one crossover [9,21,26,30] U_c, separating the weak- and strong-coupling regions, and three transitions in the U-δ plane: (i) between the AFM insulator at $\delta = 0$, marked by the heavy blue line, and the AFM metal for $\delta > 0$; (ii) $\delta_\kappa^1(U)$, separating the AFM phases with the positive and negative compressibility, which may not exist after considering the inhomogeneous phases; and (iii) $\delta_\kappa^2(U)$, from the AFM metal with negative compressibility to the PM metal. Thus, we find phase separation at small and intermediate coupling strengths, which is in agreement with the auxiliary-field QMC [27,28] and variational [21] studies. However, the phase separation occurs at intermediate doping levels in our work but at small dopings in these QMC studies. This discrepancy most likely results from the fact that the cluster slave-spin mean-field theory exaggerates the system's tendency towards a uniform AFM state, which may be remedied by enlarging the cluster size and strictly dealing with the constraint $S_\alpha^z = f_\alpha^\dagger f_\alpha - \frac{1}{2}$ locally within the cluster. It should be mentioned that U_c's at all dopings are close to the $U_{\rm Mott}$ of $\delta = 0$, manifesting that the physics in the AFM state are governed by the underlying Mott transition in the half-filled PM state [21,30,31]. The reason for the close relationship between the crossover mentioned above and the Mott transition in the PM state is that both phenomena are driven by the competition between the kinetic energy and interaction potential of the Hubbard model.

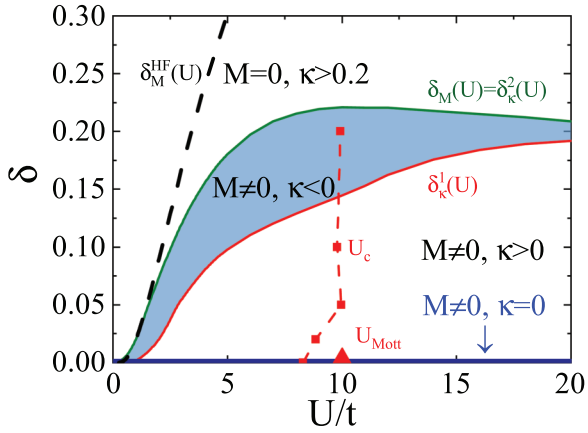

FIG. 15. The phase diagram of the Hubbard model in the U-δ plane obtained by the four-site cluster, where exist the crossover U_c (red dashed line) dividing the weak- and strong-coupling regimes, at which the $\Delta_{\rm AFM}$ is maximized, and the AFM for $U < U_c$ and $U > U_c$ is advocated by the interaction potential and kinetic energy gain, respectively. The $U_{\rm Mott}$ for the Mott transition in the PM state is marked by the red triangle. The half-filling case is highlighted by the heavy blue line, in which the system is an AFM insulator with $\kappa = 0$. Here the black dashed line represents the boundary $\delta_{\rm MF}(U)$ between the AFM and PM phases within the HF method.

IV. CONCLUSION

In summary, the cluster slave-spin method has been employed to investigate systematically the ground state properties of the single-band 2D Hubbard model on a square lattice in the parameter space of U and δ. We substantiated that the system presents a broad crossover between the weak- and strong-coupling regimes: (i) The $\Delta_{\rm AFM}$ increases monotonically with U in the weak-coupling regime, while decreases for large couplings [9]. (ii) The AFM in the weak-coupling regime is stabilized by the interaction potential gain, while that for large U is supported by the kinetic energy gain [21,30,59]. In Fig. 15 the U_c marked by the red dashed line is close to $U_{\rm Mott} = 10t$, signifying that the underlying Mott transition in the half-filled PM state dominates the properties of the AFM states by changing into a crossover [21,30,31] between the weak- and strong-coupling regimes. It is worthy mentioning that U_c at half-filling is smaller than $U_{\rm Mott}$ because of long range AFM correlations [29].

For the half-filled system, we analytically calculated in Eq. (24) the relation between M and $\Delta_{\rm AFM}$ in the small U limit, implying that the one from the HF method needs to be improved to include quantum fluctuations. After fitting the AFM gap of the cluster slave-spin data using the formula from the QMC simulation [20], and calculating the dependence of M upon U by Eq. (24), we find the result is in a good agreement with the numerical data as shown in Fig. 8.

The U-δ phase diagram was discussed in Sec. III C, from which we extracted four regimes: AFM insulator at $\delta = 0$,

AFM metal with $\kappa > 0$ and $\kappa < 0$, and the PM metal. The second-order transition occurs when the system transits from the AFM metal with $\kappa < 0$ to the PM metal phase, whereas the existence of the transition from the AFM metal phase with $\kappa > 0$ to that with $\kappa < 0$ needs to be proven further by taking the inhomogeneous states into account. Moreover, as shown in Figs. 12 and 15, the crossover, separating the weak- and strong- coupling regimes in the AFM state, always locates around $U_{\rm Mott}$, and whether this property is specifically associated with the geometry of the square lattice is worthy of subsequent investigations.

According to Figs. 2 and 9, the difference between the two- and four-site cluster results is rather quantitative than qualitative. We believe that the four-site cluster approximation is sufficient to capture the physics because its geometry obeys the same lattice symmetry as the original square lattice, which is very important to extract the reasonable solutions of the system. This conclusion can be reached in our ongoing studies on the honeycomb lattice [64].

ACKNOWLEDGMENTS

This work was supported by NSFC (No. 11774033 and No. 11974049) and Beijing Natural Science Foundation (No. 1192011). We acknowledge the support of HSCC of Beijing Normal University, and some numerical simulations in this work were performed on Tianhe in Beijing Computational Science Research Center.

APPENDIX A: RELATIONSHIP BETWEEN THE HOLON-DOUBLON CORRELATOR AND THE MOTT TRANSITION

The holon-doublon correlator [9] is defined as

$$C_{ij} = \frac{\langle N_i D_j\rangle - \langle N_i\rangle\langle D_j\rangle}{\langle N_i\rangle\langle D_j\rangle}, \tag{A1}$$

where

$$N_i = (1 - c^\dagger_{i\sigma}c_{i\sigma})(1 - c^\dagger_{i\bar\sigma}c_{i\bar\sigma}), \quad D_j = c^\dagger_{j\sigma}c_{j\sigma}c^\dagger_{j\bar\sigma}c_{j\bar\sigma}, \tag{A2}$$

which can be approximately factorized as

$$\langle c^\dagger_1 c_2 c^\dagger_3 c_4\rangle \approx \langle c^\dagger_1 c_2\rangle\langle c^\dagger_3 c_4\rangle + \langle c^\dagger_1 c_4\rangle\langle c_2 c^\dagger_3\rangle, \tag{A3}$$

leading to

$$\langle D_i\rangle \approx \langle n_{i\uparrow}\rangle\langle n_{i\downarrow}\rangle = n_{i\uparrow}n_{i\downarrow} \tag{A4}$$

$$\langle N_i D_j\rangle \approx n_{j\sigma}n_{j\bar\sigma}(\delta + n_{i\sigma}n_{i\bar\sigma}) + \sum_\sigma |\langle c^\dagger_{i\sigma}c_{j\sigma}\rangle|^2 \times\left[\frac{1}{2}|\langle C^\dagger_{i\bar\sigma}c_{j\bar\sigma}\rangle|^2 + n_{j\bar\sigma}(1 - n_{i\bar\sigma})\right]. \tag{A5}$$

Noticing that there is a simple relation between $\langle N_i\rangle$ and $\langle D_i\rangle$:

$$\begin{aligned}\langle N_i\rangle &= \langle(1 - c^\dagger_{i\sigma}c_{i\sigma})(1 - c^\dagger_{i\bar\sigma}c_{i\bar\sigma})\rangle \\ &= 1 - \sum_\sigma\langle c^\dagger_{i\sigma}c_{i\sigma}\rangle + \langle c^\dagger_{i\sigma}c_{i\sigma}c^\dagger_{i\bar\sigma}c_{i\bar\sigma}\rangle \\ &= \delta + \langle D_i\rangle,\end{aligned} \tag{A6}$$

the holon-doublon correlator C_{ij} can thus be rewritten as

$$C_{ij} \approx \frac{\sum_\sigma |\langle c^\dagger_{i\sigma}c_{j\sigma}\rangle|^2\left[\frac{1}{2}|\langle c^\dagger_{i\bar\sigma}c_{j\bar\sigma}\rangle|^2 + n_{j\bar\sigma}(1 - n_{i\bar\sigma})\right]}{(\delta + \langle D_i\rangle)\langle D_j\rangle}. \tag{A7}$$

We find from Eq. (A7) that when $U \sim U_{\rm Mott}$, the decrease of the double occupancy will enhance C_{ij} dramatically. In the case of $U \gg U_{\rm Mott}$, the double occupancy decreases at the same rate as the nearest neighbor hopping probability and more mildly than the next nearest one. Thus, the nearest neighbor holon-doublon correlator will saturate eventually and the next nearest one decrease after reaching its maximum.

APPENDIX B: ELECTRON-MOMENTUM DISTRIBUTION

Within the cluster slave-spin scheme, the electron momentum distribution $n_d^{(2/4)}(\boldsymbol{k}) = \langle d^\dagger_{\boldsymbol{k}\sigma}d_{\boldsymbol{k}\sigma}\rangle$ with respect to two/four-site cluster approximation are as follows. For the former,

$$\begin{aligned}n_d^{(2)}(\boldsymbol{k}) &\approx \frac{1}{N}\sum_j\langle f^\dagger_{j\sigma}f_{j\sigma}\rangle + \frac{\langle S^+_{j+\delta\sigma}\rangle\langle S^-_{j\sigma}\rangle}{N}\sum_{j,\delta}e^{i\boldsymbol{k}\cdot\boldsymbol{\delta}}\langle f^\dagger_{j+\delta\sigma}f_{j\sigma}\rangle \\ &= \frac{1-\delta}{2} - \frac{4Z\epsilon}{t}\gamma_{\boldsymbol{k}},\end{aligned} \tag{B1}$$

and for the latter,

$$\begin{aligned}n_d^{(4)}(\boldsymbol{k}) &\approx \frac{1}{N}\sum_j\langle f^\dagger_{j\sigma}f_{j\sigma}\rangle + \frac{\langle S^+_{j+\delta\sigma}\rangle\langle S^-_{j\sigma}\rangle}{N}\sum_{j,\delta}e^{i\boldsymbol{k}\cdot\boldsymbol{\delta}}\langle f^\dagger_{j+\delta\sigma}f_{j\sigma}\rangle \\ &\quad + \frac{\langle S^+_{j+\eta\sigma}\rangle\langle S^-_{j\sigma}\rangle}{N}\sum_{j,\eta}e^{i\boldsymbol{k}\cdot\boldsymbol{\eta}}\langle f^\dagger_{j+\eta\sigma}f_{j\sigma}\rangle \\ &= \frac{1-\delta}{2} - \frac{4Z\epsilon}{t}\gamma_{\boldsymbol{k}} \\ &\quad + \frac{4\gamma'_{\boldsymbol{k}}}{N}\sum_{\boldsymbol{k}'\in\mathrm{RBZ}}\gamma'_{\boldsymbol{k}'}\Bigg\{Z_{\rm ave}[\theta(-E^+_{\boldsymbol{k}'}) + \theta(-E^-_{\boldsymbol{k}'})] \\ &\quad + \frac{Z_\Delta}{\sqrt{(4tZ\gamma_{\boldsymbol{k}'})^2 + \Delta^2}}[\theta(-E^+_{\boldsymbol{k}'}) - \theta(-E^-_{\boldsymbol{k}'})]\Bigg\},\end{aligned} \tag{B2}$$

where

$$\gamma'_{\boldsymbol{k}} = \cos k_x\cos k_y, \quad E^\pm_{\boldsymbol{k}} = -\mu^{\rm eff} \pm \sqrt{(4tZ\gamma_{\boldsymbol{k}})^2 + \Delta^2_\sigma},$$
$$Z_{\rm ave} = \frac{|\langle\tilde z_{A\sigma}\rangle|^2 + |\langle\tilde z_{B\sigma}\rangle|^2}{2}, \quad Z_\Delta = \frac{|\langle\tilde z_{A\sigma}\rangle|^2 - |\langle\tilde z_{B\sigma}\rangle|^2}{2}.$$

To understand our present results concerning the negative and beyond unity part of this quantity around M and Γ point, we refer to the previous work on slave-particle formalism [60], where a "no-go" theorem states that the correct electron momentum distribution cannot be obtained based merely on a simple decoupling procedure for different degrees of freedom. In the work, the electron momentum distribution is expressed as

$$n_c(\boldsymbol{k},\sigma) = \frac{1-\delta}{2} + \frac{1}{N}\sum_{\boldsymbol{q}} n_{f\sigma}(\boldsymbol{k}+\boldsymbol{q})n_b(\boldsymbol{q}). \tag{B3}$$

The common feature between Eqs. (B1)–(B3) is that all of them are corrected from an average occupancy $n_\sigma = \frac{1-\delta}{2}$, and it is easy to check that our results ensure the sum rule of $N^{-1}\sum_{\boldsymbol{k}} n_d(\boldsymbol{k}) = \frac{1-\delta}{2}$.

APPENDIX C: $U(1)$ SLAVE-SPIN FORMALISM IN THE NONINTERACTING LIMIT

In this Appendix we prove analytically that in the $U(1)$ slave-spin theory [8] and within the single-site approximation, the condition $Z = 1$ at $U = 0$ recovers the correct noninteracting spinon dispersion.

Starting from the approximate Hamiltonian of a multiorbital system in the single-site approximation (Eqs. (15) and (16) in Yu and Si's work [8])

$$H_f^{\mathrm{MF}} = \sum_{k\alpha\beta}\big[\epsilon_k^{\alpha\beta}\langle\tilde{z}_\alpha^\dagger\rangle\langle\tilde{z}_\beta\rangle + \delta_{\alpha\beta}(\Delta_\alpha + \tilde{\mu}_\alpha - \lambda_\alpha - \mu)\big]f_{k\alpha}^\dagger f_{k\beta}, \tag{C1}$$

$$H_S^{\mathrm{MF}} = \sum_{\alpha\beta}\left[\epsilon^{\alpha\beta}(\langle\tilde{z}_\alpha^\dagger\rangle\tilde{z}_\beta + \langle\tilde{z}_\beta\rangle\tilde{z}_\alpha^\dagger) + \delta_{\alpha\beta}\frac{\lambda_\alpha}{2}\big(\hat{n}_\alpha^a - \hat{n}_\alpha^b\big)\right] + H_{\mathrm{int}}^S, \tag{C2}$$

where

$$\tilde{z}_\alpha^\dagger = \langle P_\alpha^+\rangle a_\alpha^\dagger b_\alpha\langle P_\alpha^-\rangle, \quad \langle P_\alpha^\pm\rangle = \frac{1}{\sqrt{1/2 \pm \big(n_\alpha^f - \frac{1}{2}\big)}},$$

$$\epsilon^{\alpha\beta} = \sum_{ij\sigma} t_{ij}^{\alpha\beta}\langle f_{i\alpha\sigma}^\dagger f_{j\beta\sigma}\rangle, \quad \epsilon_{\boldsymbol{k}}^{\alpha\beta} = \frac{1}{N}\sum_{ij} t_{ij}^{\alpha\beta} e^{i\boldsymbol{k}\cdot(\boldsymbol{r}_i - \boldsymbol{r}_j)},$$

$$\tilde{\mu}_\alpha = 2\bar{\epsilon}_\alpha\eta_\alpha, \quad \eta_\alpha = \frac{2n_\alpha^f - 1}{4n_\alpha^f\big(1 - n_\alpha^f\big)},$$

$$\bar{\epsilon}_\alpha = \sum_\beta(\epsilon^{\alpha\beta}\langle\tilde{z}_\alpha^\dagger\rangle\langle\tilde{z}_\beta\rangle + \mathrm{c.c.}). \tag{C3}$$

Equation (C2) can be rewritten as

$$H_S^{\mathrm{MF}} = \sum_\alpha\left[k_\alpha\tilde{z}_\alpha + k_\alpha^*\tilde{z}_\alpha^\dagger + \frac{\lambda_\alpha}{2}\big(\hat{n}_\alpha^a - \hat{n}_\alpha^b\big)\right] + H_{\mathrm{int}}^S, \tag{C4}$$

where $k_\alpha = \sum_\beta \epsilon^{\beta\alpha}\langle\tilde{z}_\beta^\dagger\rangle$. In the noninteracting limit, because of the decoupling of the orbits, we can keep only one degree of freedom in Eq. (C4). After dropping the crystal-field splitting Δ_α and the interaction term, the above Hamiltonians become

$$H_f^{\mathrm{MF}} = \sum_k[\epsilon_k\langle\tilde{z}^\dagger\rangle\langle\tilde{z}\rangle + (\lambda + \tilde{\mu} - \mu)]f_k^\dagger f_k, \tag{C5}$$

$$H_S^{\mathrm{MF}} = \epsilon(\langle\tilde{z}^\dagger\rangle\tilde{z} + \langle\tilde{z}\rangle\tilde{z}^\dagger) + \frac{\lambda}{2}(\hat{n}^a - \hat{n}^b), \tag{C6}$$

where $\bar{\epsilon} = 2\epsilon\langle\tilde{z}^\dagger\rangle\langle\tilde{z}\rangle$ and $\tilde{\mu} = 4\epsilon\eta\langle\tilde{z}^\dagger\rangle\langle\tilde{z}\rangle$.

Under the hard-core boson constraint: $a^\dagger a + b^\dagger b = 1$, the restricted Hillbert space is spanned by $\{|a = 1, b = 0\rangle, |a = 0, b = 1\rangle\}$, in which the slave-spin Hamiltonian (C6) has the form

$$H_S^{\mathrm{MF}} = \epsilon(\langle\tilde{z}^\dagger\rangle\tilde{z} + \langle\tilde{z}\rangle\tilde{z}^\dagger) + \frac{\lambda}{2}(\hat{n}^a - \hat{n}^b) = \begin{pmatrix} \frac{\lambda}{2} & \epsilon R\langle\tilde{z}\rangle \\ \epsilon R\langle\tilde{z}^\dagger\rangle & -\frac{\lambda}{2}\end{pmatrix}, \tag{C7}$$

with $R = \langle P_\alpha^+\rangle\langle P_\alpha^-\rangle$, which has the ground state and energy as

$$|\Psi_-\rangle = \left(\frac{-\epsilon R\langle\tilde{z}\rangle}{N}, \frac{\lambda/2 + R_0}{N}\right), \tag{C8}$$

$$E_- = -\sqrt{\frac{\lambda^2}{2} + \epsilon^2 R^2|\langle\tilde{z}^\dagger\rangle|^2}, \tag{C9}$$

where $R_0 = \sqrt{\frac{\lambda^2}{4} + \epsilon^2 R^2}$, $N = \sqrt{2R_0(\frac{\lambda}{2} + R_0)}$. Accordingly, the expectation value of $\hat{n}_a - \hat{n}_b$ and $\tilde{z}$ can be calculated as

$$\langle\hat{n}_a - \hat{n}_b\rangle = -\frac{\lambda}{2R_0}, \quad \langle\tilde{z}\rangle = -\frac{\epsilon R^2\langle\tilde{z}\rangle}{2R_0}. \tag{C10}$$

Because of the constraints $n_a - n_b = 2n^f - 1$ and $|\langle\tilde{z}\rangle|^2 = 1$ in the noninteracting case, we have

$$|\langle\tilde{z}\rangle|^2 = \frac{\epsilon^2 R^4}{4R_0^2} = 1, \tag{C11}$$

with $R = \frac{1}{\sqrt{n^f(1-n^f)}}$. Then we finally arrive at

$$\lambda = -2R_0(2n^f - 1) = \epsilon\frac{2n^f - 1}{n^f(1 - n^f)}, \tag{C12}$$

$$\tilde{\mu} = 4\epsilon\eta = \frac{4\epsilon(2n^f - 1)}{4n^f(1 - n^f)} = \epsilon\frac{(2n^f - 1)}{n^f(1 - n^f)}, \tag{C13}$$

where ϵ is negative. Thus, $\lambda = \tilde{\mu}$ in the noninteracting case ($Z = 1$) for the single orbital system, and it is straightforward to generalize the conclusion to the multiorbital systems.

[1] J. Hubbard, Proc. R. Soc. London Ser. A **276**, 238 (1963); **277**, 237 (1964).

[2] W. Langer, M. Plischke, and D. Mattis, Phys. Rev. Lett. **23**, 1448 (1969).

[3] M. Cyrot, J. Phys. France **33**, 125 (1972).

[4] F. Šimkovic, Y. Deng, N. V. Prokof'ev, B. V. Svistunov, I. S. Tupitsyn, and E. Kozik, Phys. Rev. B **96**, 081117(R) (2017).

[5] G. Kotliar and A. E. Ruckenstein, Phys. Rev. Lett. **57**, 1362 (1986).

[6] F. Lechermann, A. Georges, G. Kotliar, and O. Parcollet, Phys. Rev. B **76**, 155102 (2007).

[7] S. R. Hassan and L. de' Medici, Phys. Rev. B **81**, 035106 (2010).

[8] R. Yu and Q. Si, Phys. Rev. B **86**, 085104 (2012).

[9] W.-C. Lee and T.-K. Lee, Phys. Rev. B **96**, 115114 (2017).

[10] S. Feng, Z. B. Su, and L. Yu, Phys. Rev. B **49**, 2368 (1994); S. Feng, J. Qin, and T. Ma, J. Phys.: Condens. Matter **16**, 343 (2004); S. Feng, Y. Lan, H. Zhao, L. Kuang, L. Qin, and X. Ma, Int. J. Mod. Phys. B **29**, 1530009 (2015).

[11] M. C. Gutzwiller, Phys. Rev. **137**, A1726 (1965).

[12] T. Ogawa, K. Kanda, and T. Matsubara, Prog. Theor. Phys. **53**, 614 (1975).

[13] F. Takano and M. Uchinami, Prog. Theor. Phys. **53**, 1267 (1975).
[14] K. Chao, Solid State Commun. **14**, 525 (1974).
[15] D. Vollhardt, Rev. Mod. Phys. **56**, 99 (1984).
[16] W. Hanke and J. E. Hirsch, Phys. Rev. B **25**, 6748 (1982).
[17] R. Shankar, Rev. Mod. Phys. **66**, 129 (1994).
[18] D. Zanchi and H. Schulz, Z. Phys. B: Condens. Matter **103**, 339 (2004).
[19] S. Watanabe and M. Imada, J. Phys. Soc. Jpn. **73**, 1251 (2004).
[20] J. E. Hirsch, Phys. Rev. B **31**, 4403 (1985).
[21] L. F. Tocchio, F. Becca, and S. Sorella, Phys. Rev. B **94**, 195126 (2016).
[22] E. Vitali, H. Shi, M. Qin, and S. Zhang, Phys. Rev. B **94**, 085140 (2016).
[23] C. N. Varney, C.-R. Lee, Z. J. Bai, S. Chiesa, M. Jarrell, and R. T. Scalettar, Phys. Rev. B **80**, 075116 (2009).
[24] J. E. Hirsch, Phys. Rev. Lett. **51**, 1900 (1983).
[25] T. K. Lee and S. Feng, Phys. Rev. B **38**, 11809 (1988).
[26] A. J. Kim, F. Simkovic, and E. Kozik, Phys. Rev. Lett. **124**, 117602 (2020).
[27] C.-C. Chang and S. Zhang, Phys. Rev. B **78**, 165101 (2008).
[28] S. Sorella, Phys. Rev. B **91**, 241116(R) (2015).
[29] H. Park, K. Haule, and G. Kotliar, Phys. Rev. Lett. **101**, 186403 (2008).
[30] L. Fratino, P. Sémon, M. Charlebois, G. Sordi, and A. M. S. Tremblay, Phys. Rev. B **95**, 235109(R) (2017).
[31] L. Fratino, M. Charlebois, P. Sémon, G. Sordi, and A. M. S. Tremblay, Phys. Rev. B **96**, 241109(R) (2017).
[32] B.-X. Zheng and G. K.-L. Chan, Phys. Rev. B **93**, 035126 (2016).
[33] B.-X. Zheng, C.-M. Chung, P. Corboz, G. Ehlers, M.-P. Qin, R. M. Noack, H. Shi, S. R. White, S. Zhang, and G. K.-L. Chan, Science **358**, 1155 (2017).
[34] A. Georges, G. Kotliar, W. Krauth, and M. J. Rozenberg, Rev. Mod. Phys. **68**, 13 (1996).
[35] T. A. Maier, M. Jarrell, T. Pruschke, and M. Hettler, Rev. Mod. Phys. **77**, 1027 (2005).
[36] S. Moukouri and M. Jarrell, Phys. Rev. Lett. **87**, 167010 (2001).
[37] B. Kyung, J. S. Landry, D. Poulin, and A. M. S. Tremblay, Phys. Rev. Lett. **90**, 099702 (2003).
[38] T. Miyagawa and H. Yokoyama, J. Phys. Soc. Jpn. **80**, 084705 (2011).
[39] T. Schäfer, F. Geles, D. Rost, G. Rohringer, E. Arrigoni, K. Held, N. Blümer, M. Aichhorn, and A. Toschi, Phys. Rev. B **91**, 125109 (2015).
[40] F. Šimkovic, J. P. F. LeBlanc, A. J. Kim, Y. Deng, N. V. Prokof'ev, B. V. Svistunov, and E. Kozik, Phys. Rev. Lett. **124**, 017003 (2020).
[41] S. R. White, D. J. Scalapino, R. L. Sugar, E. Y. Loh, J. E. Gubernatis, and R. T. Scalettar, Phys. Rev. B **40**, 506 (1989).
[42] L. Vanderstraeten, J. Haegeman, and F. Verstraete, Phys. Rev. B **99**, 165121 (2019).
[43] J. E. Hirsch and S. Tang, Phys. Rev. Lett. **62**, 591 (1989).
[44] N. Furukawa and M. Imada, J. Phys. Soc. Jpn. **61**, 3331 (1992).
[45] H. J. Schulz, Phys. Rev. Lett. **64**, 1445 (1990).
[46] D. R. Penn, Phys. Rev. **142**, 350 (1966).
[47] H. Tasaki, Prog. Theor. Phys. **99**, 489 (1988).
[48] R. Zitzler, T. Pruschke, and R. Bulla, Eur. Phys. J. B **27**, 473 (2002).
[49] P. A. Lee, N. Nagaosa, and X.-G. Wen, Rev. Mod. Phys. **78**, 17 (2006).
[50] D. Greif, T. Uehlinger, G. Jotzu, L. Tarruell, and T. Esslinger, Science **340**, 1307 (2013).
[51] M. Boll, T. A. Hilker, G. Salomon, A. Omran, J. Nespolo, L. Pollet, and I. Bloch, Science **353**, 1257 (2016).
[52] L. W. Cheuk, M. A. Nichols, K. R. Lawrence, M. Okan, H. Zhang, E. Khatami, N. Trivedi, T. Paiva, M. Rigol, and M. W. Zwierlein, Science **353**, 1260 (2016).
[53] S. Feng, Phys. Rev. B **68**, 184501 (2003).
[54] S. Florens and A. Georges, Phys. Rev. B **70**, 035114 (2004).
[55] E. Zhao and A. Paramekanti, Phys. Rev. B **76**, 195101 (2007).
[56] S. Florens and A. Georges, Phys. Rev. B **66**, 165111 (2002).
[57] L. de'Medici, A. Georges, and S. Biermann, Phys. Rev. B **72**, 205124 (2005).
[58] M. Abram, J. Kaczmarczyk, J. Jedrak, and J. Spalek, Phys. Rev. B **88**, 094502 (2013).
[59] M. Qin, T. Schäfer, S. Andergassen, P. Corboz, and E. Gull, arXiv:2104.00064.
[60] S. Feng, J. B. Wu, Z. B. Su, and L. Yu, Phys. Rev. B **47**, 15192 (1993).
[61] N. Bleinstein and R. A. Handelsman, *Asymptotic Expansions of Integrals* (Dover, New York, 1986).
[62] R. Nandkishore, M. A. Metlitski, and T. Senthil, Phys. Rev. B **86**, 045128 (2012).
[63] S. R. Hassan and D. Sénéchal, Phys. Rev. Lett. **110**, 096402 (2013).
[64] M.-H. Zeng, T. Ma, and Y.-J Wang, arXiv:2109.11152.